*American Mineralogist, Volume 88, pages 352–364, 2003*

# Mineralogy, chemistry, and formation of oxidized biotite in the weathering profile of granitic rocks

**GI YOUNG JEONG* AND HYE BIN KIM**

Department of Earth and Environmental Sciences, Andong National University, Andong 760-749, South Korea

## ABSTRACT

Biotite was oxidized in deep saprolitic weathering profiles developed on granitic rocks in a humid temperate climate in the Youngju-Andong area of South Korea. The mineralogy and chemistry of these oxidized biotites were characterized by chemical analysis, electron microscopy, X-ray diffraction, thermal analysis, and radiogenic Ar analysis. The results showed that a decrease in the $b_o$-dimension, loss of radiogenic Ar, and formation of vermiculite are fairly well correlated with the degree of oxidation of ferrous iron. The chemical composition of oxidized biotite was modified by a non-stoichiometric removal of interlayer and octahedral cations to compensate for the charge imbalance induced by oxidation of Fe. The pervasive loss of cations and radiogenic Ar suggests their diffusion through oxidizing biotite in a non-expanded state. Iron oxidation and cation loss caused a decrease in the $b_o$-dimension with the formation of discontinuities that acted as conduits for the weathering solutions, resulting in partial vermiculitization (<10%). The Fe oxidation was nearly completed in the lower part of the profile, concomitant with mineralogical and chemical modification to oxidized biotite that persists throughout the profile without further notable modification. Cation release from biotite is governed in early stage by the formation of oxidized biotite, and later by its decomposition.

## INTRODUCTION

Due to its complex chemistry, Fe oxidation, diverse weathering products, and abundance in major plutonic and metamorphic rocks (Scott and Amonette 1988 and references therein), biotite weathering influences the mobility of many elements in surface environments. Major and trace elements released from biotite play an important role in the geochemical mass balance of watersheds (Velbel 1985; Berner and Berner 1996; White et al. 1998; Murphy et al. 1998), in the Sr-isotopic composition of weathering solutions, rivers, and oceans (Blum and Erel 1997; Taylor et al. 2000), and in soil nutrition (Mortland 1958; Brady 1990).

Previous studies have shown that biotite is transformed into interstratified biotite-vermiculite or into discrete vermiculite followed by a layer expansion in a saprolite-soil sequence (Velbel 1984; Banfield and Eggleton 1988; Fanning et al. 1989). The vermiculitic materials are finally decomposed into kaolin minerals and metal oxides/oxyhydroxides. However, the fact is often overlooked that a few previous studies reported the persistence of biotite throughout the weathering profile (Walker 1949; Rimsaite 1967; Gilkes et al. 1972), even in severely weathered tropical weathering profiles (Dong et al. 1998). Such biotites are characterized by a 10 Å peak in the X-ray diffraction (XRD) pattern, a yellowish-brown color, and an almost complete oxidation of Fe. This is called "oxidized biotite" hereafter.

In natural weathering environments, the occurrence of oxidized biotite in a non-expanded form may be more common than generally thought. For example, there are many reports on the direct kaolinitization of biotite without any noticeable formation of vermiculite layers (Harris et al. 1985; Rebertus et al. 1986; Kretzschmar et al. 1997; Murphy et al. 1998; Dong et al. 1998). However, these authors paid little attention to the pre-kaolinite chemical modification of biotite that probably occurs in the deeper part of the weathering profile undergoing very weak alteration. We presume here that, in most cases, the precursor of kaolinite is not fresh biotite but oxidized and chemically modified biotite.

There are several previous studies on the mineralogical and chemical modification of oxidized biotite. Rimsaite (1967) reported on the composition of oxidized biotite from very weakly weathered pegmatite, but not from a complete profile. Fordham (1990) derived the structural formula of oxidized biotite using electron microprobe analysis, but stated that his oxidized biotite was not derived from the same parent biotite as in fresh rock. Analytical transmission electron microscopy (TEM), as used by Dong et al. (1998), may not be sufficient to deduce the general formula of oxidized biotite, which has a range of chemical compositions. Gilkes et al. (1972) synthesized oxidized biotites and determined their chemical compositions. Natural oxidation of biotite is difficult to study, because of finely mixed secondary minerals (Harris et al. 1985; Rebertus et al. 1986), the uncertain oxidation state of Fe, and in some cases, a heterogeneous parent material (Scott and Amonette 1988; Fordham 1990). A systematic and comparative study is needed on a series of gradually oxidized biotites with few impurities from a

* E-mail: jearth@andong.ac.kr

complete profile crossing from fresh rock to soils, but to our knowledge this has not been done.

Granitic rocks have more homogeneous fabrics, mineralogy, and chemistry in the field than other biotite-bearing rocks, so that their weathering profiles are good candidates for a systematic study of biotite weathering. In the deep weathering profiles developed on granitoid batholiths in the Youngju-Andong area of South Korea (Fig.1), fresh biotite has weathered to oxidized biotite with very small amounts of impurities. This paper reports the mineralogical and chemical properties and formation process of these oxidized biotites, and their implications for elemental behavior in the natural weathering environments.

## GEOLOGY AND PHYSIOGRAPHY

The Jurassic granitic batholiths intruded into the Precambrian gneiss complex of the Youngnam Massif, which is composed of granitic gneiss, banded gneiss, and schist; all of these rocks in turn are overlain by Cretaceous sedimentary rocks of the Gyeongsang Basin (Fig. 1) (Hwang et al. 1999). Detailed geological mapping has shown that the batholiths consist of hornblende-biotite tonalite, biotite granodiorite, biotite granite, two-mica granites, porphyritic biotite granite, and leucocratic granite (Lee 1998; Hwang et al. 1999). The K-Ar isotopic age of the biotite from the batholiths ranges from 145 to 171 Ma (Hwang et al. 1999). The granitic rocks are medium- to coarse-grained, and locally porphyritic. They are mainly composed of plagioclase, quartz, biotite, alkali feldspar, and hornblende with accessory minerals of zircon, apatite, titanite, allanite, and ilmenite, with deuteric sericite, chlorite, and epidote (Lee 1998; Hwang et al. 1999).

The elevation of the area, including the investigated weathering profiles, ranges between 100 and 300 m, which is quite low compared with the surrounding mountain ranges that extend up to 1400 m high. Nevertheless, the study area is dominated by a well-drained mountainous topography of gentle slope (10–16°), covered with pines and deciduous vegetation. The area is located in the middle latitudes of the northern hemisphere, and belongs to the humid temperate climate zone with four distinct seasons. The mean annual air temperature and precipitation are 11.8 °C and 1050 mm, respectively. Fifty-five percent of the annual precipitation falls between June and August.

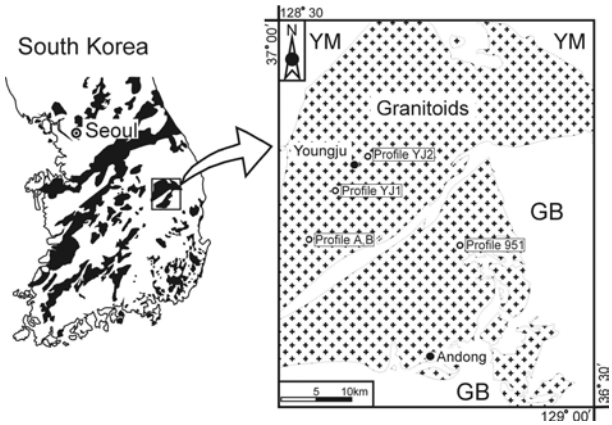


**FIGURE 1.** Distribution of granite batholiths in South Korea (areas of black color) and locations of the weathering profiles examined in this study (Profiles A, B, YJ1, YJ2, and 951). YM = Youngnam Massif, GB = Gyeongsang Basin.

## SAMPLES AND METHODS

The deep weathering profiles showing a complete variation from fresh rock to reddish-brown soil are exposed in steep walls (40–70°) formed by recent road cuts and stone quarrying. Following preliminary investigations, five weathering profiles developed in the granitic rocks (A, B, YJ1, YJ2, and 951) were selected for detailed study (Fig. 1, Table 1). Profile A is separated from Profile B by about 100 m. Fresh bedrock is exposed in the lowermost part of Profile A, but not in Profile B. As will be shown later, Profile B is a more weathered equivalent of Profile A. Samples weighing 2–3 kg were collected throughout the weathered profiles from fresh rock to the uppermost soil at intervals of 1–2 m. The whole-rock chemical compositions from Profiles A, B, YJ1, and YJ2 were determined using inductively coupled plasma (ICP) spectrometry after lithium metaborate/tetraborate fusion at Activation Laboratories Ltd. (ACTLABS), Ancaster, Canada. Samples from Profile 951 were analyzed using X-ray fluorescence spectrometry at the Korea Basic Science Institute (KBSI) in Seoul.

The weathered samples were impregnated with epoxy resin to prepare polished thin-sections following the method of Jeong and Kim (1993). Back-scattered electron (BSE) images were obtained from the thin sections using a JEOL JSM 6300 scanning electron microscope (SEM) equipped with an Oxford energy-dispersive X-ray spectrometer (EDS). The chemical compositions of the minerals were analyzed using a Cameca SX51 electron probe microanalyzer (EPMA) at the KBSI (Taejeon) under an acceleration voltage of 15 kV, a beam current of 10 nA, a beam diameter of 5 μm, and a counting time of 10 s. Biotite disks 3 mm in diameter was cut from thin sections and thinned by ion milling for TEM analysis. Lattice fringes were observed at KBSI using a Carl Zeiss EM912Ω TEM under an acceleration voltage of 120 kV. The lattice-fringe spacing was measured from digitized images by dividing the total width of neighboring fringes by the fringe number. Microchemical analysis was conducted with an Oxford EDS using *k*-factors obtained from the analysis of a biotite of known composition.

Biotite grains 0.15–0.35 mm in diameter were separated by wet sieving, magnetic separation, and hand sorting under a stereomicroscope. Although it was impossible to remove completely the fine inclusions (such as zoisite, apatite, and chlorite) from the host biotite, XRD analysis was able to detect only the very weak peaks arising from the inclusions. Color of the biotite concentrates was measured using a JS555 colorimeter of Color Techno System in L*a*b* color space of the 1976 Commission Internationale de l'Eclairage (CIE).

The biotite concentrates were further ground under acetone, and XRD patterns were obtained from the oriented samples after Mg saturation and ethylene glycol saturation, and from random samples using a Rigaku D/MAX2200 instrument equipped with a diffracted-beam monochromator and a Cu target operating at 40 kV and 30 mA. Measurement error within

**TABLE 1.** General characteristics of saprolite and soil samples from the weathering profiles

| Sample | Type (m) | DFS* | Biotite color (L*/a*/b*)† | $SiO_2$ | $Al_2O_3$ | $Fe_2O_3$ | MnO | MgO | CaO | $Na_2O$ | $K_2O$ | $TiO_2$ | $P_2O_5$ | LOI‡ | Total | LP§ (wt%) |
|---|---|---|---|---|---|---|---|---|---|---|---|---|---|---|---|---|
| B4 | Soil | –0.4 | 36.7/2.2/12.3 | 71.19 | 16.02 | 1.54 | 0.02 | 0.26 | 0.69 | 1.31 | 5.50 | 0.15 | 0.02 | 3.70 | 100.41 | 74 |
| B3 | Sap** | –1.4 | 37.2/1.9/12.4 | 61.35 | 18.09 | 4.75 | 0.06 | 1.30 | 2.33 | 1.87 | 2.60 | 0.67 | 0.13 | 6.28 | 99.42 | 46 |
| B2 | Sap | –3.2 | 35.6/1.7/10.9 | 62.29 | 18.10 | 4.59 | 0.06 | 1.53 | 3.44 | 2.43 | 2.80 | 0.67 | 0.18 | 4.12 | 100.22 | 25 |
| B1 | Sap | –5.1 | 36.1/1.6/11.2 | 60.77 | 19.19 | 4.83 | 0.06 | 1.48 | 3.02 | 2.10 | 3.04 | 0.76 | 0.18 | 5.05 | 100.46 | 34 |
| A8 | Soil | –0.1 | 35.2/1.9/10.8 | 63.96 | 17.45 | 4.52 | 0.06 | 1.44 | 3.47 | 2.60 | 2.48 | 0.70 | 0.14 | 3.90 | 100.74 | 22 |
| A7 | Sap | –0.7 | 34.5/1.7/10.0 | 63.63 | 16.52 | 4.15 | 0.06 | 1.40 | 3.63 | 2.79 | 3.10 | 0.63 | 0.16 | 2.49 | 98.55 | 18 |
| A6 | Sap | –1.5 | 34.5/1.8/10.2 | 63.84 | 17.27 | 4.46 | 0.06 | 1.54 | 4.18 | 3.22 | 2.97 | 0.66 | 0.18 | 2.15 | 100.52 | 5 |
| A5 | Sap | –2.2 | 31.7/1.6/9.2 | 58.92 | 17.63 | 6.59 | 0.09 | 2.28 | 4.45 | 3.23 | 2.93 | 1.01 | 0.27 | 2.97 | 100.37 | 1 |
| A4 | Sap | –3.7 | 34.0/1.6/9.7 | 64.56 | 16.97 | 3.90 | 0.05 | 1.37 | 4.17 | 3.42 | 3.02 | 0.60 | 0.16 | 1.73 | 99.95 | 3 |
| A3 | Sap | –4.7 | 32.9/1.0/8.1 | 66.11 | 16.38 | 4.14 | 0.06 | 1.46 | 4.27 | 3.25 | 2.46 | 0.62 | 0.17 | 1.29 | 100.20 | 3 |
| A2 | Sap | –5.0 | 28.2/1.0/4.8 | 64.80 | 17.13 | 4.07 | 0.06 | 1.49 | 4.41 | 3.47 | 2.98 | 0.60 | 0.16 | 0.93 | 100.10 | –1 |
| A1 | FRII | –5.3 | 28.9/1.0/5.1 | 66.11 | 16.43 | 4.05 | 0.05 | 1.56 | 4.44 | 3.35 | 2.83 | 0.59 | 0.15 | 0.69 | 100.25 | 0 |
| YJ1-1 | Soil | –1.3 | 35.9/2.0/11.9 | 67.38 | 17.31 | 2.96 | 0.03 | 0.62 | 0.92 | 1.32 | 3.98 | 0.34 | 0.03 | 5.45 | 100.33 | 70 |
| YJ1-2 | Sap | –2.5 | 32.2/2.1/8.9 | 65.24 | 16.99 | 4.21 | 0.06 | 1.14 | 2.89 | 2.75 | 3.10 | 0.63 | 0.13 | 3.02 | 100.14 | 24 |
| YJ1-3 | Sap | –4.2 | 33.4/2.0/9.7 | 67.29 | 15.44 | 3.81 | 0.05 | 1.10 | 3.44 | 2.91 | 2.91 | 0.55 | 0.15 | 1.83 | 99.48 | 14 |
| YJ1-4 | Sap | –5.8 | 30.1/1.3/6.4 | 67.81 | 15.46 | 3.67 | 0.05 | 1.09 | 3.67 | 3.14 | 2.88 | 0.55 | 0.15 | 1.18 | 99.64 | 8 |
| YJ1-5 | Sap | –8.2 | 32.0/1.3/8.0 | 66.89 | 16.10 | 3.90 | 0.05 | 1.15 | 3.67 | 3.22 | 3.29 | 0.55 | 0.16 | 1.41 | 100.38 | 7 |
| YJ1-6 | Sap | –10.6 | 31.8/1.3/7.8 | 66.64 | 16.17 | 3.88 | 0.05 | 1.19 | 3.82 | 3.41 | 2.79 | 0.60 | 0.15 | 1.24 | 99.94 | 2 |
| YJ1-7 | Sap | –13.7 | 29.9/0.8/5.7 | 66.52 | 16.47 | 3.79 | 0.05 | 1.15 | 3.84 | 3.44 | 3.32 | 0.53 | 0.15 | 0.97 | 100.23 | 1 |
| YJ1-8 | FR | –15.1 | 29.4/0.7/4.9 | 66.67 | 16.20 | 3.65 | 0.05 | 1.21 | 3.90 | 3.48 | 3.26 | 0.60 | 0.14 | 0.56 | 99.72 | 0 |
| YJ2-1 | Soil | –1.2 | 34.8/2.0/10.3 | 69.77 | 15.79 | 2.51 | 0.04 | 0.43 | 1.55 | 2.31 | 4.01 | 0.30 | 0.06 | 3.40 | 100.17 | 31 |
| YJ2-2 | Sap | –2.2 | 32.8/2.3/9.1 | 70.28 | 14.67 | 2.49 | 0.04 | 0.38 | 1.68 | 2.70 | 4.38 | 0.29 | 0.10 | 2.19 | 99.21 | 22 |
| YJ2-3 | Sap | –3.3 | 33.9/2.0/10.0 | 69.76 | 14.80 | 2.96 | 0.04 | 0.43 | 2.10 | 3.14 | 3.49 | 0.31 | 0.11 | 1.77 | 98.90 | 6 |
| YJ2-4 | Sap | –5.0 | 31.1/1.3/7.2 | 70.83 | 14.86 | 2.68 | 0.03 | 0.46 | 2.48 | 3.32 | 3.71 | 0.31 | 0.11 | 1.20 | 99.98 | –4 |
| YJ2-5 | Sap | –6.0 | 31.8/1.3/7.8 | 69.60 | 14.90 | 2.76 | 0.03 | 0.45 | 2.34 | 3.16 | 3.48 | 0.30 | 0.10 | 1.39 | 98.51 | 2 |
| YJ2-6 | Sap | –7.2 | 31.9/1.3/7.7 | 70.22 | 14.66 | 2.58 | 0.03 | 0.44 | 2.40 | 3.21 | 3.78 | 0.30 | 0.11 | 1.01 | 98.74 | 0 |
| YJ2-7 | Sap | –8.5 | 30.4/1.2/6.4 | 70.29 | 14.72 | 2.42 | 0.03 | 0.39 | 2.15 | 3.06 | 4.15 | 0.25 | 0.10 | 0.94 | 98.51 | 7 |
| YJ2-8 | Sap | –10.1 | 33.0/2.0/9.2 | 70.06 | 14.94 | 2.59 | 0.03 | 0.40 | 2.26 | 3.30 | 3.70 | 0.30 | 0.10 | 1.36 | 99.05 | 1 |
| YJ2-9 | FR | –12.7 | 31.0/1.0/6.3 | 71.31 | 15.01 | 2.43 | 0.03 | 0.44 | 2.31 | 3.28 | 4.19 | 0.29 | 0.10 | 0.83 | 100.23 | 0 |
| 9516 | Soil | –0.3 | 33.2/2.5/10.7 | 67.93 | 16.85 | 2.84 | 0.03 | 0.61 | 1.87 | 2.98 | 3.14 | 0.40 | 0.04 | 2.82 | 99.52 | 26 |
| 9515 | Sap | –1.0 | 30.3/1.7/7.3 | 70.50 | 15.57 | 2.45 | 0.03 | 0.51 | 2.29 | 3.31 | 2.95 | 0.34 | 0.10 | 1.50 | 99.55 | 14 |
| 9514 | Sap | –1.9 | 29.3/1.5/6.2 | 68.38 | 16.75 | 2.56 | 0.04 | 0.54 | 2.53 | 3.83 | 3.58 | 0.37 | 0.13 | 1.07 | 99.78 | 3 |
| 9513 | Sap | –3.8 | 29.6/1.6/6.4 | 69.38 | 16.13 | 2.47 | 0.04 | 0.52 | 2.51 | 3.76 | 3.44 | 0.35 | 0.12 | 1.04 | 99.74 | 4 |
| 9512 | Sap | –5.8 | 29.5/1.1/5.6 | 70.40 | 15.71 | 2.50 | 0.03 | 0.54 | 2.59 | 3.71 | 2.94 | 0.36 | 0.12 | 0.88 | 99.77 | 4 |
| 9511 | FR | –8.9 | 27.3/0.9/3.9 | 69.92 | 15.87 | 2.49 | 0.04 | 0.61 | 2.69 | 3.85 | 3.13 | 0.35 | 0.12 | 0.53 | 99.58 | 0 |
| 9425# | Sap | –0.1 | 60.4/3.1/11.8 | 66.73 | 18.58 | 4.25 | 0.05 | 0.70 | 0.36 | 0.68 | 3.76 | 0.51 | 0.02 | 7.15 | 99.78 | 84 |
| 9424# | Sap | –1.0 | 58.2/2.0/9.6 | 66.15 | 17.60 | 3.92 | 0.05 | 0.68 | 0.42 | 0.86 | 3.96 | 0.49 | 0.02 | 6.48 | 99.62 | 80 |
| 9423# | Sap | –3.0 | 58.1/1.9/9.5 | 65.63 | 17.17 | 3.96 | 0.07 | 1.03 | 1.10 | 1.66 | 3.83 | 0.51 | 0.02 | 4.80 | 99.78 | 57 |
| 9422# | Sap | –5.0 | 53.9/1.8/6.5 | 67.13 | 16.30 | 3.57 | 0.06 | 1.04 | 1.29 | 2.06 | 3.82 | 0.45 | 0.02 | 3.85 | 99.57 | 48 |
| 9421# | Sap | –6.0 | 51.4/1.5/3.9 | 69.97 | 14.70 | 3.14 | 0.04 | 1.00 | 1.91 | 3.16 | 3.85 | 0.40 | 0.02 | 1.52 | 99.71 | 22 |
| 9420# | FR | –8.0 | 50.9/1.1/2.2 | 68.09 | 14.85 | 3.29 | 0.056 | 1.05 | 2.62 | 3.84 | 3.93 | 0.388 | 0.14 | 0.66 | 98.90 | 0 |

* Depth from surface.
† L* = lightness, a* = red chroma, b* = yellow chroma in rectangular coordinates.
‡ Loss on ignition.
§ Loss of plagioclase: $\{(CaO + Na_2O)_{fresh\ rock} - (CaO + Na_2O)_{weathered\ sample}\}x100/(CaO + Na_2O)_{fresh\ rock}$.
|| Fresh rock.
# Samples from the weatherng profile of Palgongsan granite (Jeong 2000).
** Saprolite.

$2\sigma$ was ±0.008 Å for $d_{001}$, and ±0.0004 Å for $d_{060}$, respectively. Differential scanning calorimetry (DSC) and thermogravimetry (TG) were carried out for weathered biotite using a Rheometric Scientific STA1500 thermal analyzer with a sample weight of about 20 mg, and a heating rate of 10 °C/min under $N_2$ in the temperature range 20–1000 °C. Bulk-chemical compositions of the biotite concentrates were obtained by ICP analysis at ACTLABS. Their iron oxidation states were determined by Mössbauer spectroscopy at the Department of Physics, Pukyong National University. One hundred milligrams of biotite concentrate was mixed with sugar and ground under acetone according to the method recommended by Dyar and Burns (1986) to prevent preferred orientation. The radiogenic $^{40}Ar$ content of both fresh and weathered biotites was measured using a static vacuum mass spectrometer VG5400, and their K contents were analyzed using a Unicam 989 atomic absorption spectrometer at KBSI.

## RESULTS

### General characteristics of weathering profiles

The depth of the weathered profiles ranged from 5 to 15 m (Table 1). Most of the profile was saprolite, which preserves the original fabrics but loses the strength and color of fresh rock. The uppermost part of each profile (depth of 1–2 m from the surface) was altered into a brown soil where original fabrics were greatly disturbed. In the early stage of weathering, the color of biotite changes from the olive black seen in fresh rock to the yellowish brown in the saprolite and soil (Table 1). Yellow chroma of biotite was increased about two times in the

mostly weathered sample, for example from 5.1 (sample A1) to 10.8 (sample A8) in the Profile A. The parent rocks have a composition ranging from granodiorite (Profiles A and YJ1) to granite (Profiles 951 and YJ2). The biotite content in the fresh rocks ranges from 12 to 16 vol%.

The chemical compositions of the whole-rock samples are given in Table 1, which includes analysis data of samples from the Palgongsan granite (Profile 942) (Jeong 2000). The loss on ignition (LOI) increased gradually from 0.69 to 3.90 wt% in Profile A. The LOIs from Profiles YJ1, YJ2, and 951 show similar patterns to Profile A. In most of the profiles, the oxide contents did not show any significant change below about 2 m depth from the surface (DFS), but above that, CaO and $Na_2O$ decreased significantly. As most of the CaO and $Na_2O$ are assigned to plagioclase, the percentage of dissolved plagioclase could be used to assess the degree of weathering of the whole rock.

The loss of plagioclase (LP) was calculated as a weight percentage: $\{(CaO + Na_2O)_{fresh\ rock} - (CaO + Na_2O)_{weathered\ sample}\} \times 100/(CaO + Na_2O)_{fresh\ rock}$ (Table 1). The LP value can be used as a good proxy for the degree of weathering in the weakly weathered profiles. In four of the five profiles (all except Profile B), the LP value was generally lower than 10 wt% below about -2 m DFS, and above this, it rapidly increased toward the surface value of over 20 wt%. In Profile B, all the LP values were above 30 wt%, implying a severe weathering. On the other hand, in Profile 942, the LP value significantly increased at large depth in the early stage of weathering. The granitic rocks in this study are weakly weathered compared to the Palgongsan profile (Jeong 2000).

**TABLE 2.** Mineralogical data of biotite and its weathering products

| Sample | XRD | | | | | DSC-TG | |
|---|---|---|---|---|---|---|---|
| | DFS* (m) | $d_{001}$ (Å) | $d_{060}$ (Å) | $b_0$ (Å) | FWHM† (2theta) | V (wt%) | K (wt%) |
| B4 | –0.4 | 10.38 | 1.533 | 9.197 | 1.28 | 10.6 | 26.1 |
| B3 | –1.4 | 10.22 | 1.534 | 9.202 | 0.82 | 11.6 | 15.9 |
| B2 | –3.2 | 10.24 | 1.534 | 9.205 | 0.80 | 8.9 | 9.9 |
| B1 | –5.1 | 10.17 | 1.534 | 9.204 | 0.73 | 9.4 | 12.3 |
| A8 | –0.1 | 10.29 | 1.534 | 9.201 | 0.86 | 8.6 | 10.9 |
| A7 | –0.7 | 10.22 | 1.533 | 9.199 | 0.76 | 7.7 | 14.5 |
| A6 | –1.5 | 10.27 | 1.533 | 9.196 | 0.89 | 9.7 | 9.9 |
| A5 | –2.2 | 10.20 | 1.534 | 9.203 | 0.77 | 10.8 | 4.6 |
| A4 | –3.7 | 10.14 | 1.535 | 9.211 | 0.59 | 8.7 | 4.2 |
| A3 | –4.7 | 10.12 | 1.538 | 9.229 | 0.37 | 3.6 | 6.7 |
| A2 | –5.0 | 10.08 | 1.542 | 9.253 | 0.18 | 0.0 | 0.0 |
| A1 | –5.3 | 10.08 | 1.542 | 9.254 | 0.16 | 0.0 | 0.0 |
| YJ1–1 | –1.3 | 10.22 | 1.534 | 9.203 | 0.92 | 4.9 | 25.5 |
| YJ1–2 | –2.5 | 10.22 | 1.535 | 9.207 | 1.01 | 8.3 | 19.1 |
| YJ1–3 | –4.2 | 10.25 | 1.533 | 9.195 | 1.08 | 8.8 | 7.8 |
| YJ1–4 | –5.8 | 10.14 | 1.534 | 9.202 | 0.40 | 4.5 | 7.6 |
| YJ1–5 | –8.2 | 10.06 | 1.534 | 9.203 | 0.32 | 3.5 | 7.8 |
| YJ1–6 | –10.6 | 10.07 | 1.542 | 9.250 | 0.19 | 2.5 | 5.7 |
| YJ1–7 | –13.7 | 10.05 | 1.542 | 9.254 | 0.13 | 0.0 | 0.0 |
| YJ1–8 | –15.1 | 10.02 | 1.542 | 9.252 | 0.14 | 0.0 | 0.0 |
| YJ2–1 | –1.2 | 10.13 | 1.533 | 9.199 | 1.07 | 11.1 | 18.2 |
| YJ2–2 | –2.2 | 10.14 | 1.534 | 9.202 | 0.86 | 10.7 | 22.4 |
| YJ2–3 | –3.3 | 10.07 | 1.534 | 9.203 | 0.49 | 9.1 | 18.8 |
| YJ2–4 | –5.0 | 10.09 | 1.538 | 9.227 | 0.28 | 9.1 | 9.9 |
| YJ2–5 | –6.0 | 10.07 | 1.537 | 9.222 | 0.20 | 7.6 | 14.1 |
| YJ2–6 | –7.2 | 10.07 | 1.537 | 9.223 | 0.21 | 4.8 | 9.7 |
| YJ2–7 | –8.5 | 10.11 | 1.537 | 9.222 | 0.41 | 9.3 | 12.4 |
| YJ2–8 | –10.1 | 10.06 | 1.537 | 9.223 | 0.17 | 9.5 | 15.3 |
| YJ2–9 | –12.7 | 10.06 | 1.543 | 9.256 | 0.12 | 0.0 | 0.0 |
| 9516 | –0.3 | 10.12 | 1.534 | 9.201 | 0.72 | 8.0 | 13.4 |
| 9515 | –1.0 | 10.14 | 1.533 | 9.197 | 0.79 | 7.1 | 10.0 |
| 9514 | –1.9 | 10.14 | 1.534 | 9.203 | 0.40 | 6.2 | 6.9 |
| 9513 | –3.8 | 10.13 | 1.533 | 9.196 | 0.45 | 5.9 | 5.2 |
| 9512 | –5.8 | 10.13 | 1.538 | 9.226 | 0.27 | 5.7 | 7.5 |
| 9511 | –8.9 | 10.09 | 1.541 | 9.248 | 0.18 | 0.0 | 0.0 |

* Depth from surface.
† Full width at half maximum of (001) reflection.

## Biotite

**XRD.** The XRD data of the five profiles are summarized in Table 2. The XRD patterns of the biotite samples change in a systematic way with the progress of weathering: a lowering of peak height, a broadening of peak width, a low-angle shift of the (001) peak, and a high-angle shift of the (060) peak. The XRD patterns of the oriented samples from Profiles A and B are shown in Figure 2. The $d_{001}$ spacing increases gradually from 10.08 Å in fresh biotite A1 to 10.20 Å in A5, and fluctuates higher in the profile showing a maximum $d_{001}$ of 10.29 Å in the uppermost sample, A8 (Table 2). The full width at half maximum (FWHM) of the (001) peak also increases upward of the profile. After K-saturation and step-heating, the $d_{001}$ spacing of A7 gradually shifted to 10.02 Å at 550 °C, with a sharpening of the peak shape (Fig. 3). A decreasing $d_{001}$ spacing indicates the presence of a hydrous interlayer. A weak kaolinite peak at 7.3 Å disappeared at 550 °C. The $d_{060}$ spacing decreases rapidly from 1.542 Å in A1 to 1.535 Å in A4, and thereafter, decreases very gradually to 1.534 Å in A8 (Fig. 4, Table 2). In the XRD patterns of samples from Profile B, a more weathered equivalent of Profile A, the $d_{001}$ spacing varied between 10.17 and 10.38 Å. The $d_{060}$ values remained at 1.534 Å. The XRD patterns of weathered biotite in Profiles YJ1, YJ2, and 951 showed similar behavior in their shape, $d_{001}$, and $d_{060}$ characteristics.

The XRD patterns of A8, 9515, and YJ1-1 were simulated using the NEWMOD program (Reynolds 1985), with biotite and vermiculite as the two end-members. The results showed the weathered biotites to be a randomly interstratified biotite-vermiculite. The vermiculite proportions were 10% in A8 and YJ1-1, and 5% in 9515. A gradual increase in $d_{001}$ spacing and $FWHM_{001}$ upward of the profiles is ascribed to random interstratification and decreasing layer number of coherent scattering domains.

**Thermal analysis.** The DSC and TG analyses of biotite samples showed four endothermic peaks at 52–66, 155–163, 464–482, and 615–625 °C with a corresponding weight loss. The first and second endothermic peaks are from the dehydration of an adsorbed interlayer water in the vermiculite interlayer (Todor 1976). The third and fourth peaks are attributed to the dehydroxylation of kaolinite and vermiculite, respectively. The vermiculite and kaolinite contents were calculated from the weight loss of the interlayer water up to about 210 °C, and the dehydroxylation peak between 464–482 °C, respectively (Karathanasis and Harris 1994) (Table 2). As this method does not use standards, the calculated amounts of vermiculite and kaolinite are semi-quantitative. However, the data obtained in the same conditions can reasonably be interpreted to show the

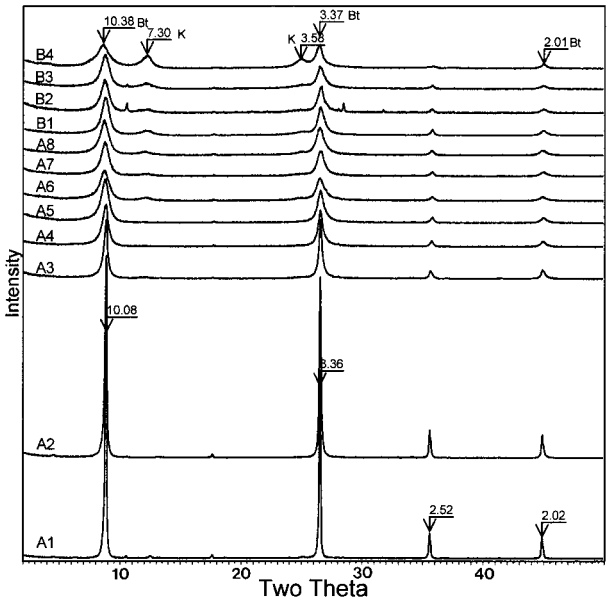


**FIGURE 2.** XRD patterns of fresh (A1) and weathered biotites (A2 to B4) in Profiles A and B. Oriented mounts. Bt = biotite, K = kaolinite. *d*-spacings in Å units.

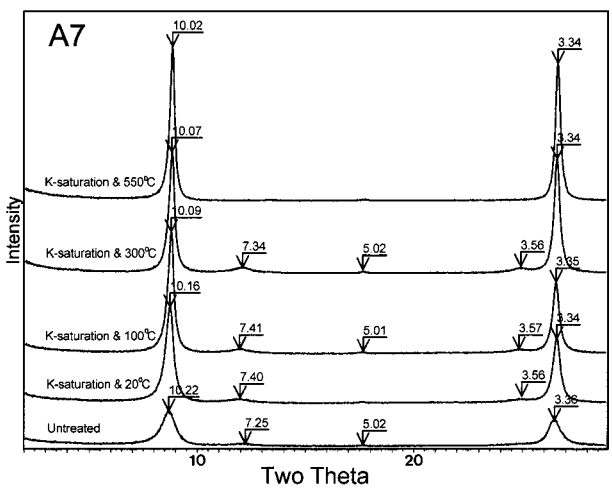


**FIGURE 3.** XRD patterns of weathered biotite (A7) heated in steps. Oriented mounts. *d*-spacings in Å units.

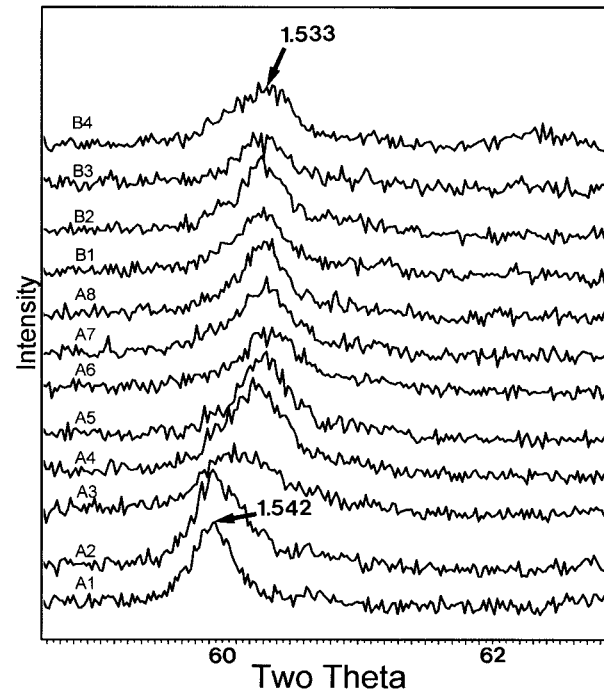


**FIGURE 4.** XRD patterns of fresh (A1) and weathered biotites (A2 to B4) in Profiles A and B. Random mounts. *d*-spacings in Å units.

variation in the mineral content of the profiles. Nevertheless, the contents of vermiculite estimated from TG analysis were similar to those obtained from the XRD pattern simulation. In Profile A, the vermiculite content rapidly increased to 9 wt% in A4 (-3.7 m) with the progress of weathering, and then remained between 8 and 11 wt% (Table 2). In Profile B, the vermiculite content remained around 10 wt%. In Profile 951, the vermiculite content gradually increased to 8 wt% (in 9516 at -0.3 m). In Profiles YJ1 and YJ2, the vermiculite content did not change after early rapid increase. Kaolinite appears together with vermiculite, but its content increases gradually, eventually exceeding vermiculite in the upper part of all the profiles (Table 2).

**Electron microscopy.** BSE images were obtained from thin sections of Profile A samples. Fresh biotite A1 shows a very homogeneous and compact texture, with scattered inclusions of apatite, hornblende, and epidote (Fig. 5a). In the slightly weathered biotite A3, the biotite had cleaved, showing loose textures with partial kaolinization and fanning (exfoliation) at the grain edges (Fig. 5b). The precipitation of kaolinite commonly occurred along the widened cleavages deep into the interior. The microtextures of A5 are similar to those of A3 (Fig. 5c). In the highly weathered biotite A8, some of the biotite grains had greatly expanded perpendicular to the cleavage plane owing to active kaolinization (Fig. 5d).

One-dimensional TEM lattice fringe images perpendicular to the *c*-axis were taken for biotite samples A1, A4, and A7 from Profile A. The fresh biotite A1 showed homogeneous textures with very thick and coherent stacks of mica layers, with only rare interstratification of chlorite layers (Fig. 6). The slightly weathered biotite A4 consists of packets of varying layer numbers (Fig. 7). The packet interfaces are mismatched, and are slightly separated in many cases, showing a mottled contrast and a buckling of the layers. A mottled contrast in sheet silicates has been ascribed to strain caused by lattice mismatch, or from a variation in cation occupancy in the interlayer region (Noe and Veblen 1999). The lattice fringes near the interfaces are larger in spacing (~11 Å) and irregular in shape. A two-layer 20 Å periodicity found near the interfaces is interpreted as a biotite-vermiculite (collapsed) pair (Kuwahara and Aoki 1995). Lattice fringe images in Figure 7 are similar to those of

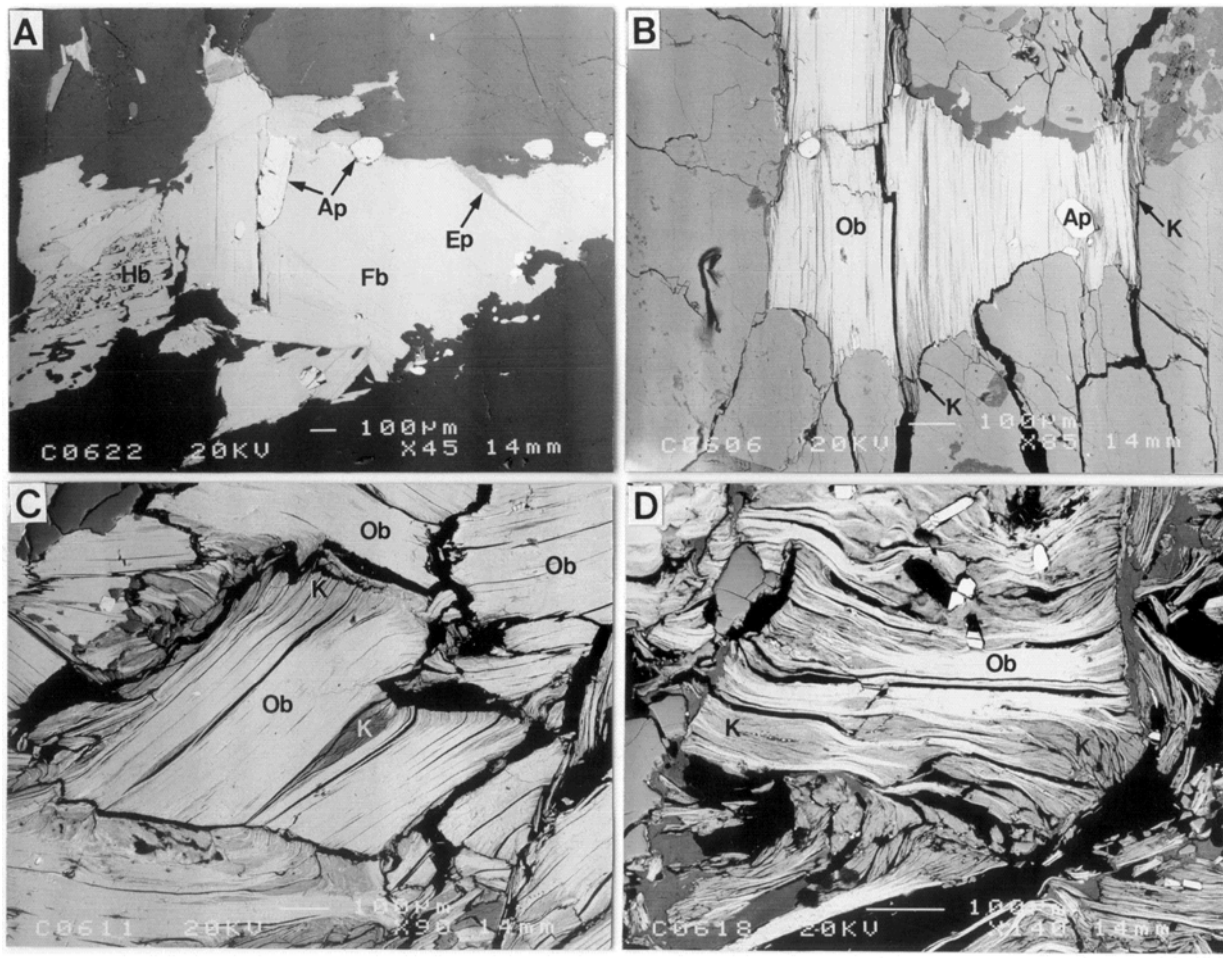


**FIGURE 5.** BSE images of thin sections of fresh and weathered biotites in Profile A. (**A**) Fresh biotite (Fb) associated with inclusions of apatite(Ap), epidote(Ep), and hornblende(Hb). Sample A1. Note compact textures of fresh biotite. (**B**) Oxidized biotite (Ob) showing widened cleavages and partial kaolinization (K) at the grain edges. Sample A3. (**C**) Oxidized biotite showing kaolinization at the edges. Sample A5. (**D**) Oxidized biotite undergoing severe kaolinization. Sample A8.

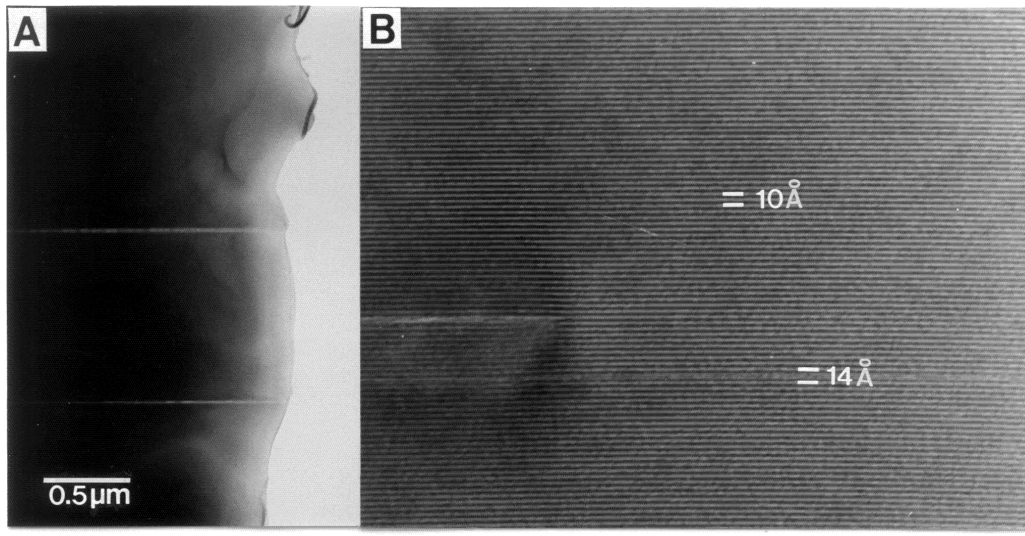


**FIGURE 6.** TEM images of fresh biotite A1. (**A**) Low magnification image. (**B**) Lattice fringes showing thick coherent stacking of 10 Å biotite layers with few 14 Å chlorite layers.

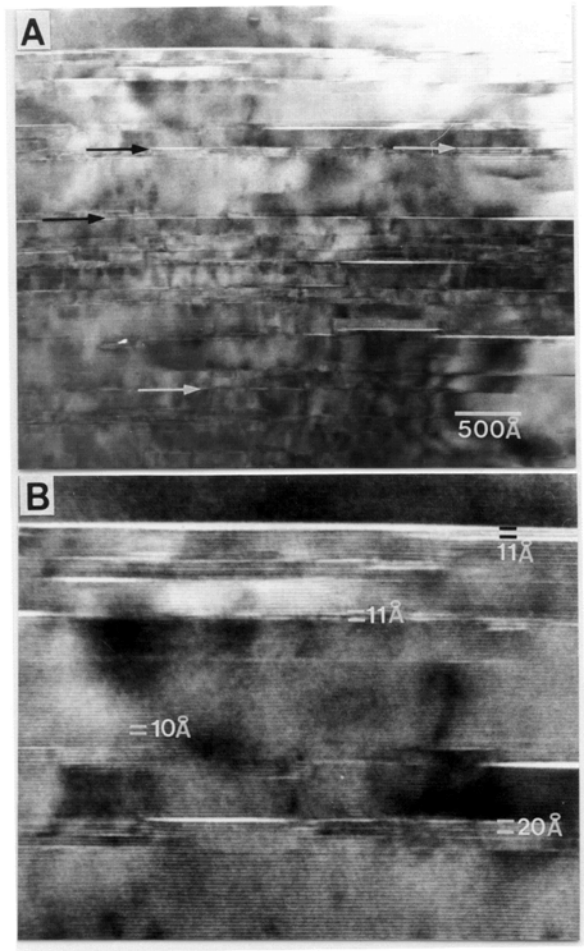


**FIGURE 7.** TEM images of oxidized biotite A4. (**A**) Abundant discontinuities (arrows) with mottled contrasts. (**B**) Magnified image showing 10 Å biotite packets of various thicknesses separated by discontinuities. Note larger spacings (~11 Å) and 20 Å periodicities associated with discontinuities.

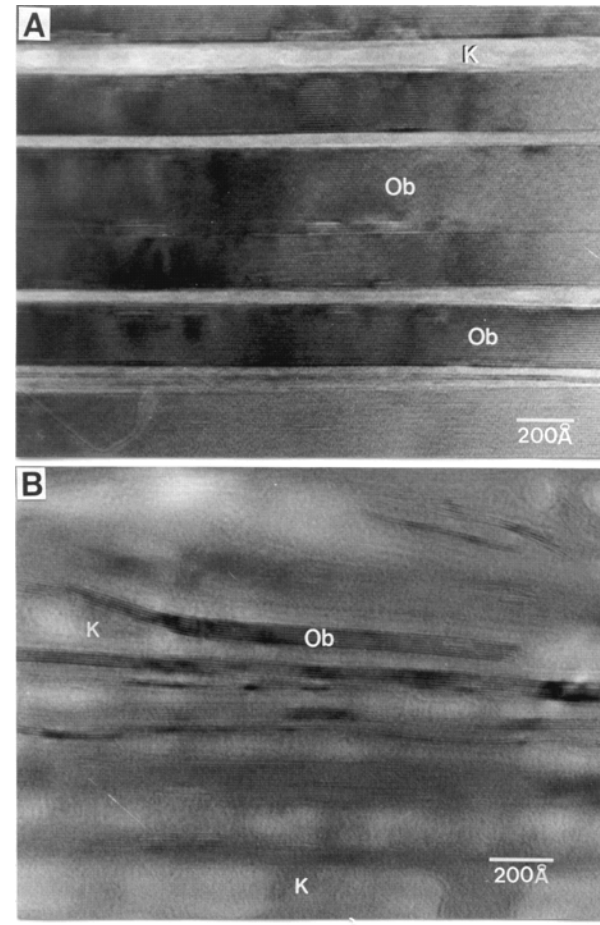


**FIGURE 8.** TEM images of oxidized biotite A7. (**A**) Biotite packets of 10 Å spacings. (**B**) Very thin and curved packets of 3–7 layers. Interstices between the oxidized biotite (Ob) packets are filled with kaolin minerals (K).

biotite undergoing early stage weathering as shown by Banfield and Eggleton (1988). However, the number of biotite layers in the packets in Figure 7 is commonly 20–30, much higher than 4–5 in their images. In the highly weathered biotite A7, kaolinite had precipitated in the cleaved spaces (Fig. 8a). Slightly curved, and very thin packets of 4–5 biotite layers were found between thick straight packets (Fig. 8b). The average spacing of the lattice fringes fell between 10.0–10.1 Å in all specimens: 10.0 ± 0.1 Å in A1, 10.1 ± 0.1 Å in A4, and 10.0 ± 0.0 Å in A7. The average spacing of the very thin biotite packets of A7, however, were 10.3 ± 0.1 Å. From the slightly larger spacing and their curved shapes, part of the very thin packets in A7 are attributed to collapsed vermiculite. The TEM images collectively confirm that most part of the oxidized biotites retain a 10 Å spacing throughout the weathering profile.

**Chemistry.** Chemical compositions of biotite concentrates from Profiles A and 951 are given in Table 3. There was a consistent decreasing trend in FeO, MgO, and $K_2O$ content that was accompanied by an increase in $Fe_2O_3$. In Profile A, the oxidation was so rapid that 80% of the total Fe was $Fe^{3+}$ in A4 (-3.7 m), whereas in Profile 951, the $Fe^{3+}$ content exceeded 80% of the total Fe in 9513 (-3.8 m). Anomalously high CaO and $P_2O_5$ contents are attributed to epidote and apatite inclusions (Fig. 5), because concentrations of these oxides are very low in the EPMA. Considering the secondary kaolinite precipitates in the weathered biotites, the oxide contents in Table 3 are probably different from those of oxidized biotite. Therefore, a reliable chemical composition of oxidized biotite was not derived using data in Table 3, even though much effort was expended to correct for any impurities.

EPMA analysis is preferred over bulk analysis for the derivation of the chemical characteristics of oxidized biotite. From the EPMA data of the fresh and weathered biotites from Profiles A and B, the numbers of cations were calculated on the basis of an anion charge of 44 (assuming all $Fe^{3+}$) are plotted against K in Figure 9, where the most prominent feature is an abrupt change in the Si/K ratios between 1.6 K and 1.7 K. A plot of Si vs. K for each sample (Fig. 10) shows that the data

**TABLE 3.** Chemical analysis data of weathered biotite from Profiles A and 951 by ICP and Mössbauer spectroscopy

| Sample | DFS (m) | $SiO_2$ | $Al_2O_3$ | FeO* | $Fe_2O_3$* | MnO | MgO | CaO | $Na_2O$ | $K_2O$ | $TiO_2$ | $P_2O_5$ | Total† | $Fe^{3+}/Fe_{total}$ |
|---|---|---|---|---|---|---|---|---|---|---|---|---|---|---|
| A8 | –0.1 | 38.22 | 19.29 | 0.13 | 18.13 | 0.20 | 7.30 | 0.59 | 0.14 | 6.62 | 2.03 | 0.08 | 92.73 | 0.99 |
| A7 | –0.7 | 37.73 | 19.08 | 0.21 | 13.63 | 0.20 | 7.19 | 0.61 | 0.16 | 6.52 | 1.93 | 0.05 | 87.31 | 0.98 |
| A6 | –1.5 | 38.34 | 18.18 | 0.45 | 18.92 | 0.21 | 7.81 | 0.79 | 0.15 | 7.39 | 2.15 | 0.08 | 94.47 | 0.97 |
| A5 | –2.2 | 38.03 | 17.11 | 0.99 | 19.44 | 0.21 | 8.05 | 1.02 | 0.16 | 7.21 | 2.24 | 0.11 | 94.58 | 0.95 |
| A4 | –3.7 | 37.57 | 16.93 | 1.87 | 18.85 | 0.22 | 8.31 | 1.10 | 0.18 | 7.43 | 2.35 | 0.11 | 94.91 | 0.90 |
| A3 | –4.7 | 37.38 | 17.33 | 6.22 | 13.28 | 0.23 | 8.50 | 0.61 | 0.16 | 8.09 | 2.30 | 0.09 | 94.19 | 0.66 |
| A2 | –5.0 | 37.44 | 16.94 | 10.59 | 9.91 | 0.27 | 9.00 | 0.64 | 0.24 | 8.81 | 2.34 | 0.10 | 96.28 | 0.46 |
| A1 | –5.3 | 36.54 | 16.96 | 16.78 | 4.50 | 0.30 | 10.08 | 0.29 | 0.16 | 9.75 | 2.56 | 0.04 | 97.96 | 0.19 |
| 9516 | –0.3 | 36.30 | 19.18 | 0.00 | 18.75 | 0.22 | 7.26 | 0.38 | 0.11 | 6.82 | 2.59 | 0.08 | 91.69 | 1.00 |
| 9515 | –1.0 | 36.31 | 17.48 | 0.38 | 19.51 | 0.23 | 7.52 | 0.87 | 0.10 | 7.42 | 2.70 | 0.22 | 92.74 | 0.98 |
| 9514 | –1.9 | 35.52 | 16.12 | 3.43 | 17.68 | 0.26 | 8.18 | 0.81 | 0.11 | 7.96 | 2.88 | 0.20 | 93.16 | 0.82 |
| 9513 | –3.8 | 34.95 | 15.91 | 2.88 | 14.50 | 0.27 | 7.89 | 1.03 | 0.12 | 7.14 | 2.87 | 0.20 | 87.76 | 0.82 |
| 9512 | –5.8 | 36.08 | 16.39 | 6.87 | 14.84 | 0.28 | 8.28 | 1.00 | 0.10 | 8.18 | 2.87 | 0.23 | 95.12 | 0.66 |
| 9511 | –8.9 | 36.07 | 16.34 | 17.81 | 4.59 | 0.35 | 9.43 | 0.52 | 0.13 | 9.54 | 3.14 | 0.14 | 98.05 | 0.19 |

* Oxidation state was determined with Mössbauer spectroscopy.
† Loss on ignition was not determined by the very low quantity of samples.

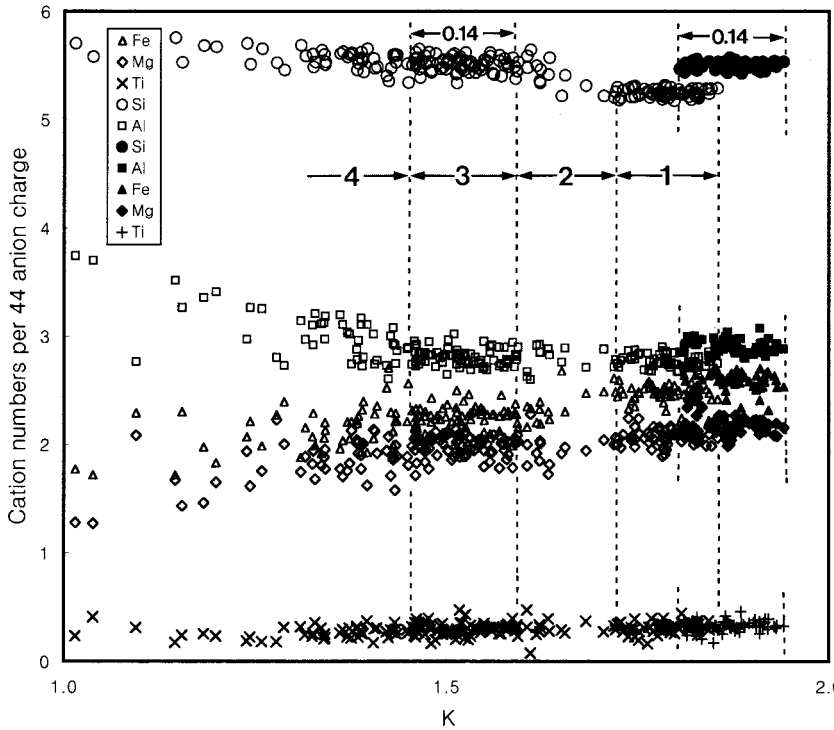


**FIGURE 9.** Plot of cation numbers vs. K, calculated on the basis of an anion charge of 44, assuming all $Fe^{3+}$ from EPMA data of all the samples (A1–A8, B1–B4) from Profiles A and B (open and × symbols). The EPMA data of sample A1 and part of A2 were recalculated after partitioning the Fe using the Fe oxidation state of the fresh biotite A1 in Table 3 (solid and + symbols). The data points (assuming all $Fe^{3+}$) have been divided into four regions, which are discussed in the text.

for A1 have the lowest Si/K ratio, those for A4 to A8 have high Si/K ratios, and the data for A2 and A3 span the entire range of Si/K ratios. The change in the Si/K ratios coincides with the degree of Fe oxidation, as shown in Table 3, where 90% of the total Fe was $Fe^{3+}$ in A4. It is clear that these tiered distributions (Fig. 9) are artifacts of the structural formula calculation that assumes all $Fe^{3+}$. The cation numbers of all the data for A1 and part of that for A2 in the low Si/K tier of Figure 10 were recalculated after partitioning the Fe using the ratio of 81($Fe^{2+}$):19($Fe^{3+}$) in the fresh biotite A1 (Table 3), and added to Figure 9. The Si/K ratios before oxidation are mostly the same as those of A4 to A8 after oxidation (Fig. 9).

Because the tetrahedral sheet of biotite is more stable than the octahedral and interlayer sites, it is unreasonable to expect a radical change in the tetrahedral composition during the early stages of weathering at low temperature (Newman and Brown 1966; Gilkes et al. 1972). Therefore, the preservation of the Si number during weathering is reasonable. Thus, the change in the Si/K ratios of data (assuming all $Fe^{3+}$) in Figure 9 provides information on the change in Fe oxidation state at the onset of weathering.

The data points in Figure 9 have been divided into four regions on the basis of a change in distribution pattern with decreasing K: (1) a horizontal region of fresh biotite; (2) an inclined region comprising a fine-scale mixture of fresh and oxidized biotite; (3) a horizontal region of oxidized biotite; and (4) an inclined region comprising a fine-scale mixture of oxidized biotite and kaolinite. The width of region 3 was set to 0.14, the same as the width of fresh biotite after correction for Fe oxidation state, under the assumption that K loss due to Fe oxidation is proportional to the original K content of each analysis point. This assumption is reasonable, as shown in the widths

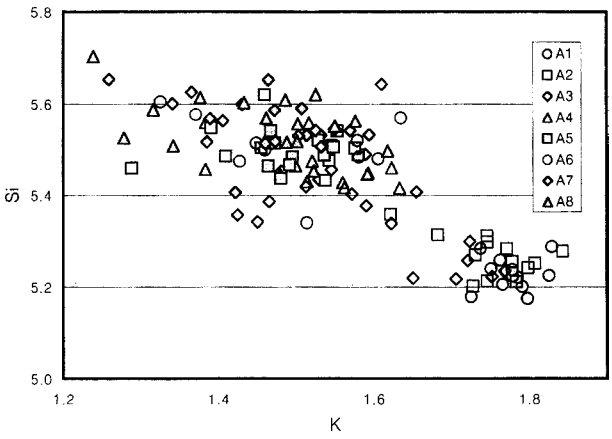


**FIGURE 10.** Plot of Si vs. K in biotite, calculated on the basis of an anion charge of 44, assuming all $Fe^{3+}$, from EPMA data of samples A1–A8 in Profile A.

of the flat regions in plots of Si, Al, Fe, and Mg vs. depth (Fig. 9). In region 4, Si and Al increase with decreasing K, while Fe, Mg, and Ti decrease. From Figure 9, the location of region 3 was determined to be between 1.46–1.60 K. The average structural formula of oxidized biotite could be calculated from data in region 3.

The EPMA data from Profiles 961 and YJ1 also show similar distribution patterns, and can be treated in the same way as above. However, the EPMA data from Profile YJ2 showed a continuous distribution that is probably due to a high $Fe^{3+}$ content in the fresh biotite, and so could not be used to derive a structural formula. Three sets of structural formulae of fresh and oxidized biotites from three weathering profiles are given in Table 4. For comparison, the microareas of biotite packets (about 200 nm in diameter) that were free of kaolinite packets and goethite aggregates in A7 were also analyzed using TEM-EDS. Although more scattered than the corresponding EPMA data, the resulting structural formula averaged from 24 analyses was very similar to that derived from the EPMA data (Table 4). The method given here is a reliable procedure for deriving a representative structural formula of naturally oxidized biotite.

From a comparison of the structural formulae given in Table 4, there is no significant change in tetrahedral site occupancy, but oxidized biotite has released 11–16% $Fe_{total}$ and 4–12% Mg from the octahedral sheet, and 15–19% K from the interlayer position. The sum of the octahedral cations decreased by 11–13%, with increasing dioctahedral characteristics and decreasing interlayer charge of 13–16%. Radoslovich (1962) related the chemical composition of micas to their $b_0$-dimension using regression analysis. Using Radoslovich's approach and the structural formulae from this study, the $b_0$-dimensions have been calculated to be 9.196 Å (Profile A), 9.200 Å (Profile 951), and 9.204 Å (Profile YJ1), respectively, which correspond fairly well to the measured values in Table 2.

The XRD results show that the weathered biotite includes 5–10% vermiculite. The formula in Table 4 is actually that of a randomly interstratified biotite (oxidized) vermiculite. It is impossible to extract only the oxidized biotite composition from this formula. Inevitably, this may be the limit of current chemical analysis techniques. The very slight increase in the number of Ca cations by about 0.03 indicates the presence of vermiculite with a high cation exchange capacity. If interlayer K were completely removed from the biotite layer to form vermiculite, the removed K during the formation of oxidized biotite would be 11% (Profile A), 5% (Profile YJ1), and 13% (Profile 951), respectively, after a vermiculite correction of 10% (Pro-

**TABLE 4.** Structural formulas of fresh and oxidized biotites on the basis of 44 negative charges

| | Profile A | | | | | Profile 951 | | | | Profile YJ1 | | | |
|---|---|---|---|---|---|---|---|---|---|---|---|---|---|
| | Fresh biotite (EPMA) | Oxidized biotite (EPMA) | gain(+) loss(-) | Change* % | Oxidized biotite (TEM) | Fresh biotite (EPMA) | Oxidized biotite (EPMA) | gain(+) loss(-) | Change* % | Fresh biotite (EPMA) | Oxidized biotite (EPMA) | gain(+) loss(-) | Change* % |
| Si | 5.50 | 5.51 | 0.02 | 0 | 5.53 | 5.48 | 5.47 | –0.01 | 0 | 5.48 | 5.43 | –0.05 | –1 |
| $^{IV}$Al | 2.50 | 2.49 | –0.02 | –1 | 2.47 | 2.52 | 2.53 | 0.01 | 0 | 2.52 | 2.57 | 0.05 | 2 |
| Sum | 8.00 | 8.00 | 0.00 | | 8.00 | 8.00 | 8.00 | 0.00 | | 8.00 | 8.00 | 0.00 | |
| $^{IV}$Al | 0.40 | 0.32 | –0.08 | | 0.31 | 0.29 | 0.26 | –0.03 | | 0.38 | 0.22 | –0.16 | |
| $Fe^{2+}$ | 2.08 | | – | | 0.00 | 2.24 | 0.00 | – | | 2.05 | 0.00 | – | |
| $Fe^{3+}$ | 0.50 | 2.24 | – | | 2.11 | 0.52 | 2.32 | – | | 0.68 | 2.44 | – | |
| $Fe_{total}$ | 2.58 | 2.24 | –0.35 | –13 | 2.11 | 2.75 | 2.32 | –0.43 | –16 | 2.73 | 2.44 | –0.29 | –11 |
| Mg | 2.17 | 1.98 | –0.19 | –9 | 1.94 | 2.11 | 1.86 | –0.26 | –12 | 1.96 | 1.88 | –0.08 | –4 |
| Ti | 0.33 | 0.30 | –0.03 | | 0.43 | 0.34 | 0.34 | –0.01 | | 0.32 | 0.27 | –0.05 | |
| Mn | 0.04 | 0.03 | –0.01 | | 0.00 | 0.04 | 0.03 | –0.01 | | 0.04 | 0.04 | –0.01 | |
| Sum | 5.52 | 4.87 | –0.65 | –12 | 4.79 | 5.55 | 4.81 | –0.74 | –13 | 5.44 | 4.85 | –0.59 | –11 |
| Ca | 0.01 | 0.04 | 0.03 | | 0.00 | 0.01 | 0.04 | 0.03 | | 0.00 | 0.03 | 0.02 | |
| Na | 0.02 | 0.01 | –0.01 | | 0.00 | 0.02 | 0.03 | 0.00 | | 0.03 | 0.01 | –0.02 | |
| K | 1.87 | 1.51 | –0.36 | –19 | 1.61 | 1.88 | 1.55 | –0.33 | –17 | 1.89 | 1.61 | –0.28 | –15 |
| K† | | | –0.20† | –11† | | | | –0.25† | –13† | | | –0.10† | –5† |
| Charge | 1.91 | 1.60 | –0.31 | –16 | 1.61 | 1.92 | 1.65 | –0.27 | –14 | 1.93 | 1.67 | –0.26 | –13 |
| | Element ratio | | | | | Element ratio | | | | Element ratio | | | |
| $Fe_{total}$/Mg | 1.19 | 1.13 | 1.83 | | | 1.30 | 1.25 | 1.70 | | 1.39 | 1.30 | 3.56 | |
| K/Mg | 0.86 | 0.76 | 1.92 | | | 0.89 | 0.83 | 1.28 | | 0.96 | 0.86 | 3.47 | |
| K/Mg† | | | 1.04† | | | | | 0.96† | | | | 1.27† | |

* Change relative to fresh biotite.
† Correction of vermiculte content: 10% in Profiles A and YJ1, and 5% in Profile 951.

files A and YJ1) and 5% (Profile 951) (Table 4). A significant difference in octahedral composition is not expected between closely interstratified oxidized biotite and vermiculite formed from the same parent biotite. The formula after correction for vermiculite content in Table 4 is likely to approximate that of oxidized biotite.

**Radiogenic argon.** The radiogenic $^{40}$Ar/K atomic ratio of weathered biotites provides constraints on the behavior of interlayer K during oxidation. The ratio of the biotites in Profile A decreases rapidly from $11.7 \times 10^{-7}$ in A1 to $5.2 \times 10^{-7}$ in A4, and is then nearly constant in the more weathered biotite with 55% loss of original radiogenic $^{40}$Ar (Table 5). The $^{40}$Ar/K ratio of the biotites from Profile 951 gradually decreases from $13.5 \times 10^{-7}$ in 9511 to $3.6 \times 10^{-7}$ in 9516 with a 73% loss of radiogenic $^{40}$Ar. In Profile B, the ratio does not show a great change between $3.3 \times 10^{-7}$ and $4.4 \times 10^{-7}$. From Profiles A, B, and 951, the radiogenic $^{40}$Ar tends to decrease rapidly with the initiation of weathering, and then to slow down with the progress of weathering.

## DISCUSSION

Because Profile B is considered to be a more-weathered equivalent of Profile A, both profiles can be combined to form a continuous series covering a wider range of weathering degrees, and investigated in more detail than the others. The changes in the mineralogical and chemical properties of the biotites with depth in Profiles A and B are summarized in Figure 11 for discussion below.

### Mineralogical and chemical modification

Mineralogical and chemical modification of fresh to oxidized biotite are nearly completed in the lower part of the Profile A (samples A1 to A4), and persist throughout the Profile A and B. Oxidized biotite was the major phase of weathered biotite in all the profiles studied. The persistence of oxidized biotite confirms its enhanced K-retention capability (Gilkes 1973), which has been attributed to the change in orientation of octahedral hydroxyl resulting in the decrease of repulsion between hydroxyl proton and interlayer K (Barshad and Kishk 1968; Gilkes et al. 1973). Oxidized biotite is different from pedogenic biotite formed by K-fixation of vermiculite in the surface soil horizons (Nettleton et al. 1973; Tarzi and Protz 1979; Ghabru et al. 1987). Gradual development of the oxidized biotites in the weathered profiles provides a chance to analyze the chemical change in the oxidation of biotite. Table 4 shows that, with the oxidation of $Fe^{2+}$, the cations were preferentially removed from the octahedral and interlayer sites of the biotite resulting in the slight modification of chemical composition. The $Fe_{total}$:Mg atomic ratio in the removed fraction was 1.83 (Profile A), 1.70 (Profile 951), and 3.56 (Profile YJ1), respectively. Because the ratio is 1.19(A1), 1.30(9511), and 1.39(YJ1–1) in the fresh biotites, the removal of $Fe_{total}$ is greater than that of Mg. The K:Mg atomic ratios in the removed fraction were 1.04 (Profile A), 0.96 (Profile 951), and 1.27 (Profile YJ1), which is similar to the ratios of 0.86(A1), 0.89(9511), and 0.96(YJ1-1), respectively, in fresh biotite equivalents (Table 4). The order of non-stoichiometric removal of cations is Fe > Mg ≅ K. The radiogenic Ar loss is correlated linearly with Fe oxidation (Fig. 11), implying that interlayer or octahedral vacancies, which formed after the removal of cations, became pathways for Ar mobilization. The Ar loss occurs concomitantly with those of other cations, but the neutral charge of the Ar atom greatly enhances its release (up to 73%), in contrast to the cations that are subject to Coulombic forces.

The weathered biotite is a random interstratifcation of oxidized biotite (>90%) and vermiculite (<10%), with very minor kaolinite. The content of vermiculite does not show any significant variation in the profile after its early formation (Fig. 11, Table 2). The variation in vermiculite content matches the variation in radiogenic $^{40}$Ar loss and percentage of $Fe^{3+}$, and is inversely correlated with the $b_o$ dimension and yellow chroma (Fig. 11, Tables 2, 3, and 5). The formation of vermiculite layers is likely related to the formation of discontinuities along the cleavages of oxidized biotite (Figs. 5, 7, and 8). Gilkes et al. (1972) observed exfoliation of biotite to finer flakes after the artificial oxidation of biotite. Ferrow et al. (1999) found an exfoliation of biotite flakes after acid leaching. In natural samples, Fordham (1990) showed exfoliation of fine flakes of several micrometers thickness from the oxidizing biotite. However, the origin of the discontinuities and exfoliation was not studied in detail. Banfield and Eggleton (1988) suggested that

**TABLE 5.** Radiogenic argon data of weathered biotites from Profiles A, B, and 951

| Sample | DFS (m) | K (wt%) | $^{36}$Ar (×10$^{-10}$ccSTP/g) | $^{40}Ar_{radiogenic}$ (×10$^{-8}$ccSTP/g) | Uncertainty | Ar/K atom ratio (×10$^{-7}$) | Loss of $^{40}Ar_{radiogenic}$ (%)* |
|---|---|---|---|---|---|---|---|
| B4 | –0.4 | 3.324 | 193.00 | 835.29 | 2.93 | 4.39 | 62 |
| B3 | –1.4 | 4.820 | 413.13 | 916.68 | 9.64 | 3.32 | 72 |
| B2 | –3.2 | 5.155 | 326.54 | 1044.04 | 3.76 | 3.54 | 70 |
| B1 | –5.1 | 5.184 | 365.01 | 1164.94 | 6.04 | 3.92 | 66 |
| A8 | –0.1 | 5.008 | 223.20 | 1534.76 | 18.44 | 5.35 | 54 |
| A7 | –0.7 | 5.260 | 222.05 | 1705.18 | 4.14 | 5.66 | 52 |
| A6 | –1.5 | 5.762 | 268.77 | 1732.58 | 3.16 | 5.25 | 55 |
| A5 | –2.2 | 5.528 | 268.87 | 1384.42 | 4.02 | 4.37 | 63 |
| A4 | –3.7 | 5.608 | 223.98 | 1677.83 | 3.08 | 5.22 | 55 |
| A3 | –4.7 | 6.347 | 221.00 | 2416.19 | 4.81 | 6.64 | 43 |
| A2 | –5.0 | 6.843 | 141.77 | 3742.27 | 23.70 | 9.55 | 18 |
| A1 | –5.3 | 7.678 | 27.03 | 5139.09 | 14.90 | 11.68 | 0 |
| 9516 | –0.3 | 5.174 | 277.64 | 1072.74 | 4.90 | 3.62 | 73 |
| 9515 | –1.0 | 5.543 | 230.61 | 1654.54 | 16.00 | 5.21 | 61 |
| 9514 | –1.9 | 6.209 | 195.30 | 2433.97 | 3.88 | 6.84 | 49 |
| 9513 | –3.8 | 5.902 | 254.64 | 2920.08 | 10.15 | 8.64 | 36 |
| 9512 | –5.8 | 6.099 | 135.01 | 3208.08 | 5.07 | 9.18 | 32 |
| 9511 | –8.9 | 6.631 | 185.87 | 5137.41 | 6.25 | 13.52 | 0 |

* Loss of argon: $\{(^{40}Ar_{radiogenic}/K)_{fresh\ biotite} - (^{40}Ar_{radiogenic}/K)_{weathered\ biotite}\} \times 100/(^{40}Ar_{radiogenic}/K)_{fresh\ biotite}$.

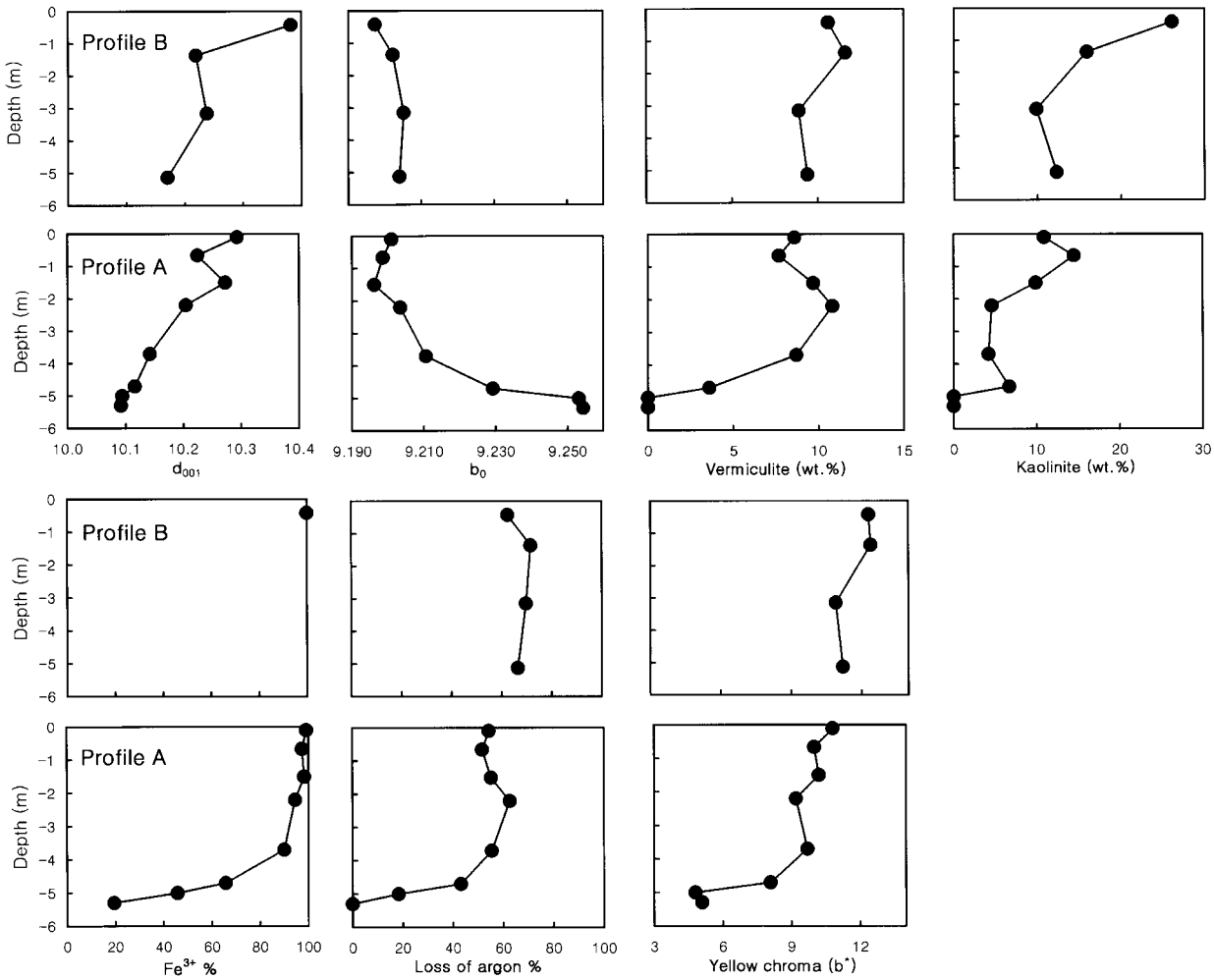


**FIGURE 11.** Summary diagrams showing the mineralogical and chemical changes of biotite in Profiles A and B. Profile B is a more-weathered equivalent of Profile A. Iron oxidation state was not determined for samples B1–B3.

growth of single vermiculite layer may distort the surrounding structure, thus inhibiting vermiculitization of adjacent biotite layers and promoting interstratification of vermiculite with 4–5 biotite layers. In our study, layer numbers of oxidized biotite packets are much larger than those in their TEM images, and the packet interfaces are likely widened cleavages rather than single vermiculite layers (Fig. 7). Banfield and Eggleton (1988) observed dissolution cavities in the early weathering of biotite, which was interpreted to supply space for vermiculitization of biotite (requiring a volume increase), but we have not found any dissolution cavities in the early stage of weathering. We conclude that, in our samples, vermiculitization was preceded by the formation of discontinuities. The mottled contrast of oxidized biotite (Fig. 7) most likely denotes strain accumulated during weathering. This strain may be caused by a decrease in cell dimensions owing to Fe oxidation and the ejection of $Fe^{3+}$ and $Mg^{2+}$, which would result in a $b_0$-dimension contraction of 0.5–0.6%. Although the change in the one biotite layer is very small, it may subsequently accumulate in stacked layers. When the strain reaches a critical value, it may be released by the formation of discontinuities along the cleavages. The interfacial discontinuities created during oxidation may be a conduit for solutions, and the exposed surface and a few adjacent biotite layers would be preferentially vermiculitized. The further formation of vermiculite would be limited after the completion of oxidation, because of resistance of oxidized biotite against further leaching of interlayer K.

The kaolinite content shows a pattern similar to the vermiculite content, but shows a slight upward increase in the profile. Kaolinitization of biotite has been studied by many authors (Harris et al. 1985; Rebertus et al. 1986; Banfield and Eggleton 1988; Kretzschmar et al. 1997; Dong et al. 1998). Banfield and Eggleton (1988) observed lattice fringe images of biotite undergoing late-stage weathering and suggested dissolution of biotite followed by epitactic precipitation of kaolinite on remaining biotite. As suggested by Jeong (1998), however, exfoliation at the kaolinizing grain edges (Figs. 5b, 5c, and 5d) can be ascribed to a massive epitactic precipitation of kaolinite from weathering solutions introduced externally into the cleaved space of the vermiculite, because the Al content in biotite is not sufficient to form a large amount of kaolinite. Therefore, most of the Si and Al for kaolinite formation did not originate

internally from the oxidation of biotite, but externally from weathering solutions that migrated downward from higher in the profile. Plagioclase is likely the major source of Al and Si for kaolinite. Vermiculite formation is limited after its early formation, because vermiculite inherits its structure from the parent biotite, but precipitation of kaolinite from solution could be continued in the cleaved spaces within oxidized biotites, so its content could continuously increase upward in the profile (Fig. 11, Table 2). Oxidized biotite supplied templates for epitactic precipitation of kaolinite as well as being a minor source of Si and Al by its decomposition.

### Oxidation mechanism

Several mechanisms have been suggested to balance the excess positive charge caused by the oxidation of Fe: release of interlayer cations, loss of structural hydroxyl (deprotonation), and ejection of octahedral Fe (Rimsaite 1970; Farmer et al. 1971; Ross and Rich 1974; Scott and Amonette 1988). In their extensive review of previous work, Scott and Amonette (1988) concluded that deprotonation of oxidized biotite in a natural weathering environment is uncertain. The present study shows that the loss of interlayer K and octahedral Fe and Mg was sufficient to balance the excess charge without requiring deprotonation (Table 4). This mechanism is also supported by the analysis of biotite oxidized artificially (Gilkes et al. 1972). Although deprotonation is a major charge-balancing mechanism in thermal oxidation (Rimsaite 1970: Rancourt et al. 2001), cation ejection is likely to be more important in low-temperature weathering environments.

Our data show that oxidized biotite with 10 Å spacing gradually develops from fresh biotite without pervasive vermiculitization. It is different from the generally accepted oxidation mechanism. For sufficient oxidation of biotite, many experiments have used strong oxidants, such as $H_2O_2$ and $Br_2$ in combination with salt solutions, like NaCl and sodium tetraphenyl boron, to extract interlayer K and to expand the biotite layer, because an expanded interlayer helps to accelerate oxidation (Newman and Brown 1966; Farmer et al. 1971; Ross and Rich 1974; Scott and Youssef 1978; Amonette et al. 1985). The final weathering products were mostly vermiculite or interstratified biotite–vermiculite in varying orders and proportions. Farmer et al. (1971) suggested that Fe oxidation proceeds through initial vermiculitization, the entry of oxygen, the oxidation and then ejection of Fe, and finally collapse due to re-adsorption of K. Gilkes et al. (1972), however, artificially synthesized oxidized biotite with 10 Å spacing, only with a hot bromine oxidant treatment of fresh biotite in a sealed capsule.

White and Yee (1985) showed that dissolved $Fe^{3+}$ may oxidize $Fe^{2+}$ in biotite via a coupled electron transfer and cation release. This process occurs at the solution-water interface, and may be difficult to explain pervasive oxidation in a non-expanded state. Considering a non-expansion of oxidized biotite, Ar and cations should be removed by a diffusion process through the biotite lattice. Although the process of Fe oxidation in a non-expanded state is uncertain (Scott and Amonette 1988), we think that it requires a diffusion process of the oxidants. Oxygen is a very weak oxidant compared with $H_2O_2$, $Br_2$, and HOCl, but is a major oxidant in natural environments. Very slow inward diffusion of the oxygen molecule may occur through the interlayer or the hexagonal holes of the tetrahedral sheet of non-expanded biotite concomitant with the outward diffusion of Fe, Mg, K, and Ar. However, considering the long geological time needed for the development of deep saprolitic weathering profiles, which generally exceed several million years in a humid temperate climate (Pavich 1986), the very slow diffusion of $O_2$ may oxidize Fe in biotite even in weathering solutions that are more dilute than salt solutions in a laboratory.

### Implications to elemental behavior in the weathering profile

Although dissolution experiments have been conducted on fresh biotite (Acker and Bricker 1992; Kalinowski and Schweda 1996; Taylor et al. 2000), there has been no systematic dissolution study of naturally oxidized biotite. Oxidized biotite is likely to be more common than has been believed previously, as discussed in the Introduction. The biotites undergoing direct weathering to kaolinite are not fresh biotite, but are pre-oxidized biotites in the deep part of the weathering profile. Normal mineralogical analysis of saprolite and soils does not distinguish oxidized from fresh biotite in parent rock, and also, little attention is paid to oxidized biotite in very weakly weathered rock at the bottom of a profile, leading to an underestimation of the oxidized biotite content. In some environments, oxidized biotite is a major contributor to the pore water chemistry of weathering profiles on biotite-rich bedrock (White et al. 1998). If oxidized biotite is widespread in weathering profiles, a dissolution experiment is needed for naturally oxidized biotite.

The biotite weathering process identified in this study suggests a release pattern of cations throughout the profile. Biotite transforms into oxidized biotite, followed by mineralogical and chemical modification at an early stage of weathering, and then persists throughout the weathering profiles with partial kaolinitization in the highly weathered part of the profile. In this case, it is expected that cation release from biotite occurs in two ways: (1) a non-stoichiometric release of Fe, Mg, and K in the lower part of the profile, forming an oxidized biotite; and (2) the pervasive release of most of its cations during decomposition higher in the profile.

## ACKNOWLEDGMENTS

The manuscript was improved by the comments of M.A. Velbel, J. Price, and one anonymous reviewer. We thank C.S. Lee for Mössbauer spectroscopy, J.M. Kim for radiogenic Ar analysis, and J.H. Bae for XRD analysis. This work was funded by the Korea Research Foundation (project no. KRF–2000–015–DP0433).

## REFERENCES CITED

Acker, J.G. and Bricker, O.P. (1992) The influence of pH on biotite dissolution and alteration kinetics at low temperature. Geochimica et Cosmochimica Acta, 56, 3073–3092.

Amonette, J., Ismail, F.T., and Scott, A.D. (1985) Oxidation of iron in biotite by different oxidizing solutions at room temperature. Soil Science Society of America Journal, 49, 772–777.

Banfield, J.F. and Eggleton, R.A. (1988) Transmission electron microscope study of biotite weathering. Clays and Clay Minerals, 36, 47–60.

Barshad, I. and Kishk, F. (1968) Oxidation of ferrous iron in vermiculite and biotite alters fixation and replaceability of potassium. Science, 162, 1401–1402.

Berner, E.K. and Berner, R.A. (1996) Global Environment: Water, Air, and Geochemi-

cal Cycles, 376 p. Prentice Hall, Upper Saddle River, New Jersey.
Brady, N.C. (1990) The Nature and Properties of Soils, 621 p. Macmillan, New York.
Blum, J.D. and Erel, Y. (1997) Rb-Sr isotope systematics of a granitic soil chronosequence: The importance of biotite weathering. Geochimica et Cosmochimica Acta, 61, 3193–3204.
Dong, H., Peacor, D.R., and Murphy, S.F. (1998) TEM study of progressive alteration of igneous biotite to kaolinite throughout a weathered soil profile. Geochimica et Cosmochimica Acta, 62, 1881–1888.
Dyar, M.D. and Burns, R.G. (1986) Mössbauer spectral study of ferruginous one-layer trioctahedral micas. American Mineralogist, 71, 955–965.
Fanning, D.S., Keramidas, V.Z., and El-Desoky, M.A. (1989) Micas. In Dixon, J.B. and S. B. Weed, Eds., Minerals in Soil Environments, p. 551–633. Soil Science Society of America, Madison, Wisconsin.
Farmer, V.C., Russell, J.D., McHardy, W.J., Newman, A.C.D., Ahlrichs, J.L., and Rimsaite, J.Y.H. (1971) Evidence for loss of protons and octahedral iron from oxidized biotites and vermiculites. Mineralogical Magazine, 38, 121–137.
Ferrow, E.A., Kalinowski, B.E., Veblen, D.R., and Schweda, P. (1999) Alteration products of experimentally weathered biotite studied by high-resolution TEM and Mössbauer spectroscopy. European Journal of Mineralogy, 11, 999–1010.
Fordham, A.W. (1990) Formation of trioctahedral illite from biotite in a soil profile over granite gneiss. Clays and Clay Minerals, 38, 187–195.
Ghabru, S.K., Mermut, A.R., and St. Arnaud, R.J. (1987) The nature of weathered biotite in sand-sized fractions of gray luvisols (Boralfs) in Saskatchewan, Canada. Geoderma, 40, 65–82.
Gilkes, R.J. (1973) The alteration products of potassium depleted oxybiotite. Clays and Clay Minerals, 21, 303–313.
Gilkes, R.J., Young, R.C., and Quirk, J.P. (1972) The oxidation of octahedral iron in biotite. Clays and Clay Minerals, 20, 303–315.
———(1973) Artificial weathering of oxidized biotite: I. Potassium removal by sodium chloride and sodium tetraphenylboron solutions. Soil Science Society of America Proceedings, 37, 25–28.
Harris, W.G., Zelazny, J.C., Baker, J.C., and Martens, D.C. (1985) Biotite kaolinitization in Virginia Piedmont soils: I. Extent, profile trends, and grain morphological effects. Soil Science Society of America Journal, 49, 1290–1297.
Hwang, S.K., Kim, S.W., Chang, T.W., Kim, J.M., and Lee, S.K. (1999) Intrusive phases and igneous processes in the Yeongju batholith. Economic and Environmental Geology, 32, 669–688. (in Korean with English abstract)
Jeong, G.Y. (1998) Vermicular kaolinite epitactic on primary phyllosilicates in the weathering profiles of anorthosite. Clays and Clay Minerals, 46, 509–520.
———(2000) The dependence of localized crystallization of halloysite and kaolinite on primary minerals in the weathering profile of granite. Clays and Clay Minerals, 48, 196–203.
Jeong, G.Y. and Kim, S.J. (1993) Boxwork fabric of halloysite-rich kaolin formed by weathering of anorthosite in Sancheong area, Korea. Clays and Clay Minerals, 41, 56–65.
Kalinowski, B.E. and Schweda, P. (1996) Kinetics of muscovite, phlogopite, and biotite dissolution and alteration at pH 1–4, room temperature. Geochimica et Cosmochimica Acta, 60, 367–386.
Karathanasis, A.D. and Harris, W.G. (1994) Quantitative thermal analysis of soil materials. In Amonette, J.E. and Zelazny, L.W., Eds., Quantitative methods in soil mineralogy, p. 360–411. Soil Science Society of America, Madison, Wisconsin.
Kretzschmar, R., Robarge, W.P., Amoozegar, A., and Vepraskas, M.J. (1997) Biotite alteration to halloysite and kaolinite in soil-saprolite profiles developed from mica schist and granite gneiss. Geoderma, 75, 155–170.
Kuwahara, Y. and Aoki, Y. (1995) Dissolution process of phlogopite in acid solutions. Clays and Clay Minerals, 43, 39–50.
Lee, B.H. (1998) Petrology of granitic rocks in the Andong area. M.S. thesis, Andong National University, Andong, Korea, 72 p. (in Korean)
Mortland, M.M. (1958) Kinetics of potassium release from biotite. Soil Science Society of America Proceedings, 22, 503–508.
Murphy, S.F., Brantley, S.L., Blum, A.E., White, A.F., and Dong, H. (1998) Chemical weathering in a tropical watershed, Luquillo Mountains, Puerto Rico: II. Rate and mechanism of biotite weathering. Geochimica et Cosmochimica Acta, 62, 227–243.
Noe, D.C. and Veblen, D.R. (1999) Mottled contrast in TEM images of mica crystals. American Mineralogist, 84, 1932–1938.
Nettleton, W.D., Nelson, R.E., and Flach, K.W. (1973) Formation of mica in surface horizons of dryland soils. Soil Science Society of America Proceedings, 37, 473–478.
Newman, A.C.D. and Brown, G. (1966) Chemical changes during the alteration of micas. Clay Minerals, 6, 297–310.
Pavich (1986) Process and rates of saprolite production and erosion on a foliated granitic rock of the Virginia Piedmont. In Colman, S.M. and Dethier, D.P., Eds., Rates of Chemical Weathering of Rocks and Minerals, p. 551–590. Academic Press, Orlando, Florida.
Radoslovich, E.W. (1962) Cell dimensions and symmetry of layer lattice silicates. American Mineralogist, 47, 617–636.
Rancourt, D.G., Mercier, P.H.J., Cherniak, D.J., Desgreniers, S., Kodama, H., Robert, J.-L., and Murad, E. (2001) Mechanisms and crystal chemistry of oxidation in annite: resolving the hydrogen-loss and vacancy reactions. Clays and Clay Minerals, 49, 455–491.
Rebertus, R.A., Weed, S.B., and Buol, S.W. (1986) Transformation of biotite to kaolinite during saprolite-soil weathering. Soil Science Society of America Journal, 50, 810–819.
Reynolds, R.C. Jr. (1985) NEWMOD, a computer program for the calculation of one-dimensional diffraction pattern of mixed-layered clays. R.C. Reynolds Jr., 8 Brook Dr., Hanover, New Hampshire.
Rimsaite, J. (1967) Biotites intermediate between dioctahedral and trioctahedral micas. Clays and Clay Minerals, 15, 375–393.
———(1970) Structural formulae of oxidized and hydroxyl-deficient micas and decomposition of the hydroxyl group. Contribution to Mineralogy and Petrology, 25, 225–240.
Ross, G.J. and Rich, C.I. (1974) Effect of oxidation and reduction on potassium exchange of biotite. Clays and Clay Minerals, 22, 355–360.
Scott, A.D. and Amonette J. (1988) Role of iron in mica weathering. In Stucki, J.W. and U. Schwertmann, U., Eds., Iron in soils and clay minerals, p. 537–625. Reidel, Dordrecht, The Netherlands.
Scott, A.D. and Youssef, A.F. (1978) Structural iron oxidation during mica expansion. International Clay Conference Proceedings, Oxford, 1, 17–26.
Tarzi, J.G. and Protz, R. (1979) Increased selectivity of naturally weathered biotites for potassium. Soil Science Society of America Journal, 43, 188–191.
Taylor, A.S., Blum, J.D., Lasaga, A.C., and MacInnis, I.N. (2000) Kinetics of dissolution and Sr release during biotite and phlogopite weathering. Geochimica et Cosmochimica Acta, 64, 1191–1208.
Todor, D.N. (1976) Thermal Analysis of Minerals, 256 p. Abacus Press, Kent, England.
Velbel, M.A. (1984) Weathering processes of rock-forming minerals. In Fleet, M.E, Ed., Short Course in Environmental Geochemistry, p. 67–111. Mineralogical Association of Canada, London, Ontario, Canada.
———(1985) Geochemical mass balances and weathering rates in forested watersheds of the southern Blue Ridge. American Journal of Science, 285, 904–930.
Walker, G.F. (1949) The decomposition of biotite in the soil. Mineralogical Magazine, 28, 693–703.
White, A.F. and Yee, A. (1985) Aqueous oxidation-reduction kinetics associated with coupled electron-cation transfer from iron-containing silicates. Geochimica et Cosmochimica Acta, 49, 1263–1275.
White, A.F., Blum, A.E., Schulz, M.S., Vivit, D.V., Stonestrom, D.A., Larsen, M., Murphy, S.F., and Eberl, D. (1998) Chemical weathering in a tropical watershed, Luquillo Mountains, Puerto Rico: I. Long-term versus short-term weathering fluxes. Geochimica et Cosmochimica Acta, 62, 209–226.

MANUSCRIPT RECEIVED APRIL 6, 2002
MANUSCRIPT ACCEPTED SEPTEMBER 24, 2002
MANUSCRIPT HANDLED BY GERALD GIESTER